

## Chapter 7

### Fabrication and Performance: CIGS Solar Cell Module

#### 7.0 Motivation, Objective, and Abstract

##### Motivation

An imprint of various CIGS solar cell deposition technique have been cognizance for accomplishing near theoretical limits and reducing the gap between cell and module efficiency. Meticulously, advances in cost-effective deposition techniques of all functional layer and substrate modification are always drives the prime attention. Yielding high quantum efficiency and reducing the radiation-free recombination are a progressively path forward.

##### Objective

- To optimize the fabrication process for developing CIGS solar cell and 50 x 50 mm of CIGS solar cell module.
- To fabricate the Finger Grid mask of different sizes using Nd:YAG 1064 nm Laser.
- To analyze the performance of CIGS solar cell under different deposition conditions of CdS buffer and intrinsic i-ZnO layer and 50 x 50 mm CIGS solar cell module.

##### *Abstract*

*Copper Indium Gallium Diselenide (CIGS) solar cell module have been fabricated on 50 x 50 mm Soda-lime glass substrate. The fabrication process for developing CIGS solar cell module have been optimized using the Physical Vapour Deposition of all functional layers except the buffer layer. CdS-buffer layer have been deposited using the Chemical Bath Deposition technique (CBD). Using Nd:YAG 1064 nm Laser on 0.1 mm of copper sheet, Al-Finger grid have been patterned. Performance of CIGS solar cell were studied using buffer layer deposited with thermal, chemical bath, and RF sputtering deposition techniques. CdS-CBD layer with variable deposition duration and*

*the RF sputtered i-ZnO layer was also optimized. Quantum efficiency response and performance of 50 x 50 mm of CIGS solar cell module were estimated.*

## **7.1 Fabrication Process of CIGS solar cell Module**

Fabrication of CIGS solar cell module requires detailed knowledge and understanding of growth mechanism, deposition techniques, physics of operation of device, and skill of analyzing the characteristics and performance of the cell and module [1]. In the present work, the stack of multilayer SLG/Mo/CIGS/CdS/i-ZnO/AZO was deposited sequentially to develop CIGS solar cell module as shown in Fig. 7.1.

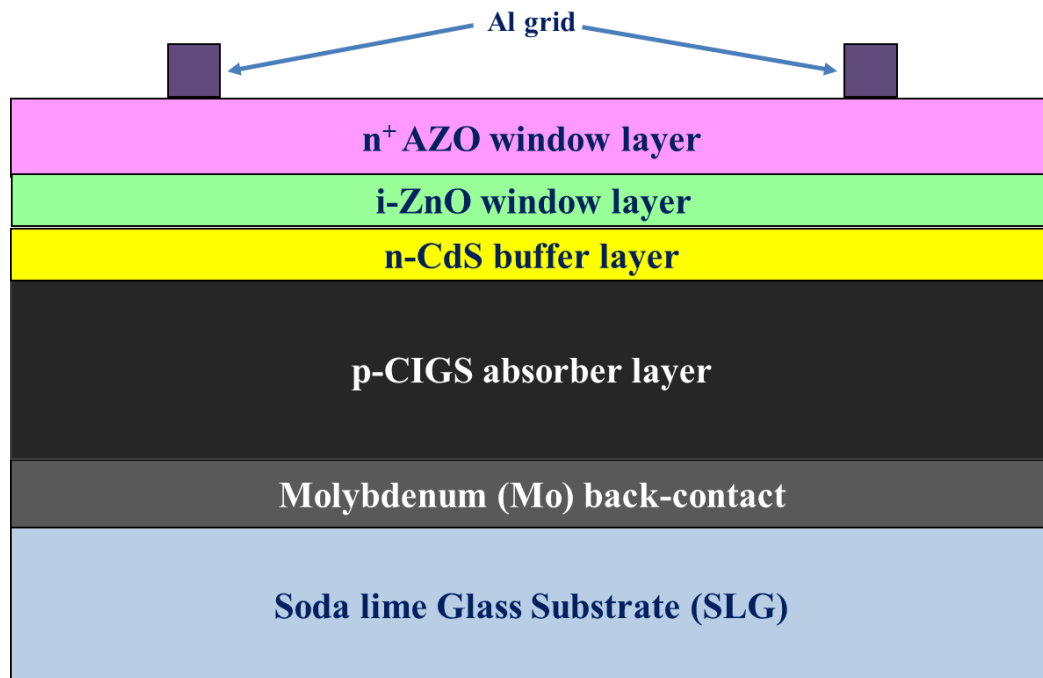


**Fig. 7.1: Schematic of the stack of multilayer SLG/Mo/CIGS/CdS/i-ZnO/AZO CIGS solar cell.**

The physics of operation of the photovoltaic device are governed by five mechanisms of converting photons to electrical carriers. The mechanisms are (1) absorption of photons, (2) generation of carriers, (3) diffusion of minority carriers towards the edge of depletion, (4) separation of minority carriers by the electric field, and (5) carriers collection at the front contact. To perform these mechanisms each layer of the multilayer stack as mentioned in Fig. 7.1 has a dedicated role. The capabilities of each layer to perform is dependent on the deposition techniques. Here, all layers have been grown using PVD techniques

except the buffer layer. Commencing with optimizing each layer parameters suitable for the fabrication of CIGS solar cell, inclusively deposition parameters were analyzed. Techniques such as Direct Current (DC) sputtering, Radio Frequency (RF) sputtering, and Chemical Bath Deposition were optimized for the deposition of each layer. Table 7.1 lists the optimized thickness and deposition temperature parameter of each layer used to develop the CIGS solar cell module.

**Table 7.1: Deposition Technique, Temperature, and Thickness of functional layers of CIGS Solar cell module.**

<b>Layers</b>	<b>Deposition Technique</b>	<b>Substrate temperature</b>	<b>Thickness of the film (nm)</b>
<b>Mo</b>	<b>DC magnetron sputtering</b>	<b>RT</b>	<b>1000</b>
<b>CIGS</b>	<b>RF magnetron sputtering</b>	<b>RTA at 400 °C (2 mins) + 550 °C (8 mins)</b>	<b>1500</b>
<b>CdS</b>	<b>Chemical Bath Deposition</b>	<b>70 °C</b>	<b>80</b>
<b>ZnO</b>	<b>RF magnetron sputtering</b>	<b>RT</b>	<b>i-ZnO = 50</b>
			<b>Al-ZnO = 450</b>
<b>Al Grid</b>	<b>DC magnetron sputtering</b>	<b>RT</b>	<b>500</b>

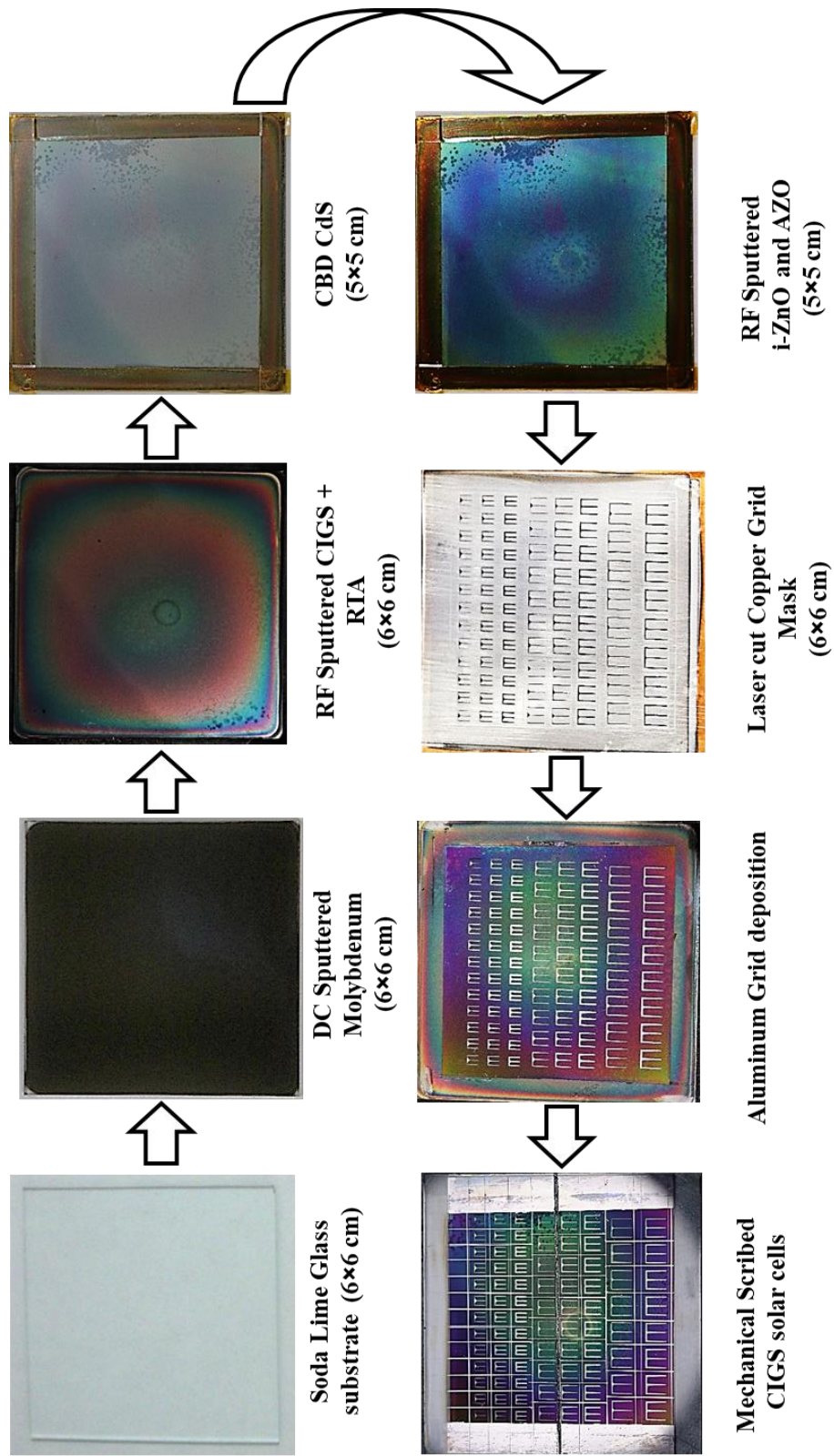
On a 60 x 60 mm Soda Lime Glass (SLG) glass substrate, the sequence of depositions of the functional layers was carried out as mentioned in the above list. Before the deposition, the SLG substrate has been processed with organic and plasma cleaning. Fig. 7.2 describes the sequence of the fabrication steps to develop a multilayer SLG/Mo/CIGS/CdS/i-ZnO/AZO/Al. CIGS solar cell using DC sputtering, RF sputtering, and Chemical Bath Techniques. During the CBD deposition process, Kapton tape has adhered on the periphery of SLG/Mo/CIGS layers covering 5 mm width. This prevents the Mo layer to be covered by the CdS buffer layer during the CBD process. For charge collection, the Aluminum (Al) grid of the ‘Finger’ pattern of different sizes using the DC sputtering technique has been deposited. The size of the grid has an important role in charge collection, therefore, Finger grids of 50  $\mu\text{m}$ , 100  $\mu\text{m}$ , and 200  $\mu\text{m}$  have been deposited. All three different size of the Finger grid mask has patterned in-house on a 0.1 mm thick copper sheet by Nd:YAG 1064 nm laser shown in Fig.

7.3. Finally, each cell of a different area  $9 \text{ mm}^2$ ,  $16 \text{ mm}^2$ , and  $25 \text{ mm}^2$  has been isolated using a mechanical scribing process.

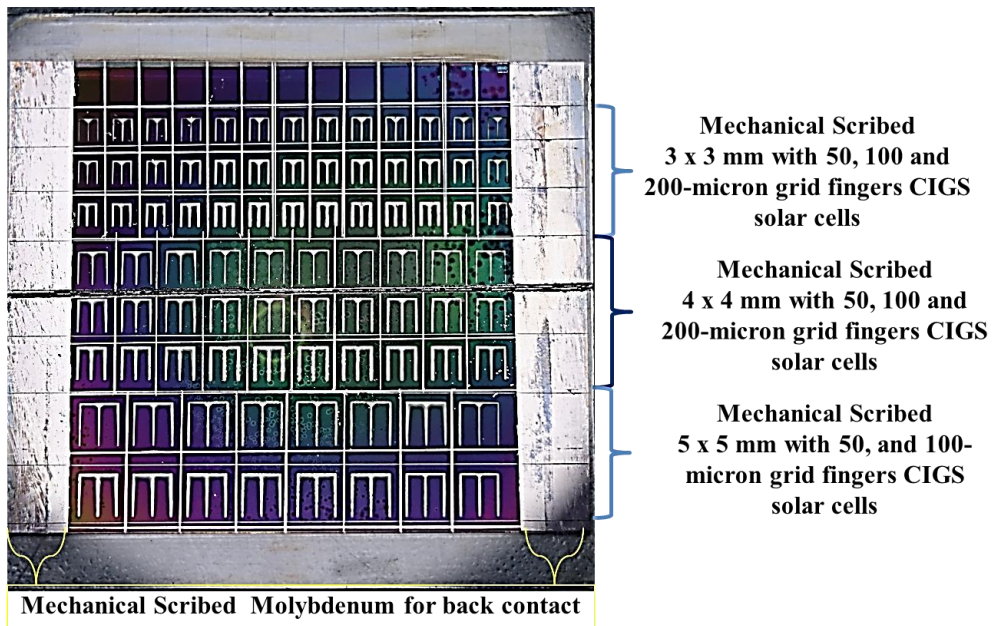
The growth of multilayered CIGS solar is a spectacle when focused on using Field Emission Scanning Electron Microscopy (FESEM). Individual layers stacked as per Fig. 7.1 and Fig. 7.2 are manifested in Fig. 7.4. The thickness of each layer has also been estimated which is in agreement with Table 7.1. The back contact Mo layer has columnar growth with a thickness of 980 nm, absorber layer CIGS has channelized grain growth with a thickness of  $1.5 \text{ }\mu\text{m}$ . 77 nm buffer CdS layer and 53 nm of the high resistive transparent i-ZnO layer was observed. It seems difficult to visualize both layers explicitly with naked eyes. Finally, the top window layer AZO with a thickness of 474 nm was observed.

From the cell to module development, the fabrication process adds a few more steps to be performed. Monolithic integration of the CIGS solar cell module into series of cells has been carried out using the Laser patterning process. The laser patterning (P1, P2, and P3) has been processed at three different levels during the deposition sequence. This patterning process connects the adequate region of front and back contact of adjacent cells; thus, it reduces the contact resistance and dead zone area. This patterning merits for the dispensable use of wires, tabs, metal grids, ribbons which reduces the effect of shading and hinders the module performance. Fig. 7.5 describes a schematic of the complete sequence of deposition and patterning process to develop the CIGS solar cell module.

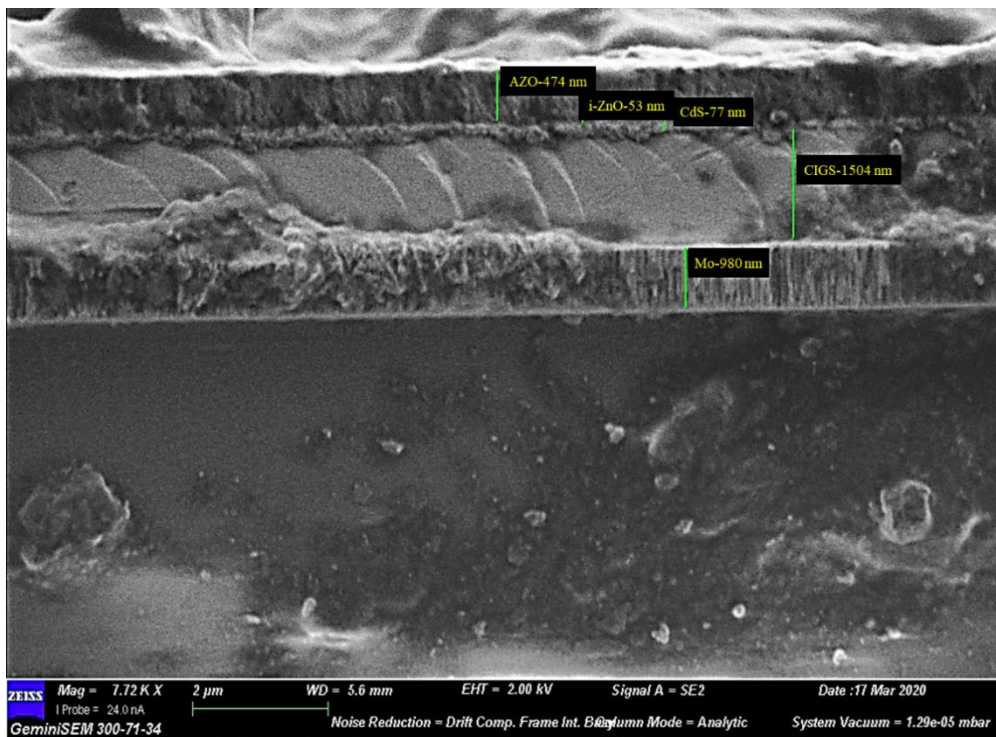
Monolithically CIGS solar cell module has been integrated via following deposition and patterning process mentioned in Fig. 75. Laser Patterning P1 was carried out after deposition of ohmic back contact Mo layer using Nd:YAG 1064 nm laser. An effort was made for P2 laser patterning using 532 nm laser after the deposition buffer CdS layer. The clean P2 patterning still has challenged over the module area. The possible reason may be the compatibility of laser features for the Lift-off process during the P2 process or there may be inhomogeneity and non-uniformity of the deposited layers. So, the alternative



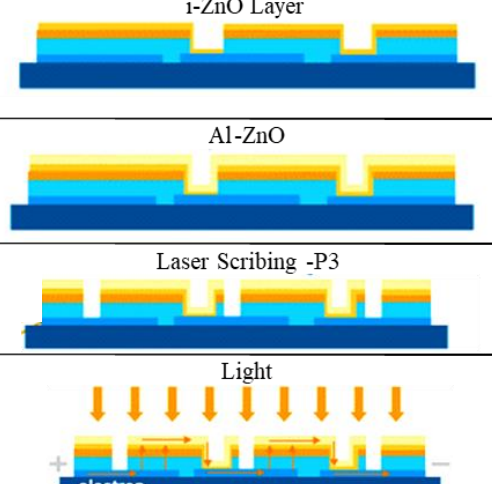
**Fig. 7.2: Fabrication steps of CIGS thin-film Solar Cells.**



**Fig. 7.3:** Photograph of 50  $\mu\text{m}$ , 100  $\mu\text{m}$ , and 200  $\mu\text{m}$  in size Al Finger grid on multilayer SLG/Mo/CIGS/CdS/i-ZnO/AZO CIGS solar cell.



**Fig. 7.4:** FESEM image of multilayered CIGS solar cell.

	Cleaning
	DC magnetron sputtering
	Laser scribing of Mo layer
	RF sputtering
	CBD process.
	Laser scribing of CIGS and CdS layer
	RF sputtering
	RF sputtering layer followed laser scribing
	Making individual solar cells.
	Current flows in CIGS solar cells

**Fig. 7.5: Schematic of the cell to module process of CIGS solar cell module.**

conventional method i. e. mechanical scribing was adopted for P2 patterning [2]. A fine needle was used for P2 patterning. P3 patterning of top window contact available at our laboratory. So, for P3 patterning, a mechanical scribing technique was used. Fig. 7.6 represents the fabrication steps of a monolithically integrated thin-film CIGS solar cell module on a 60 x 60 mm area. Fig. 7.7 is the close view of the P1 laser scribed, P2, and P3 mechanically scribed CIGS solar cell module.

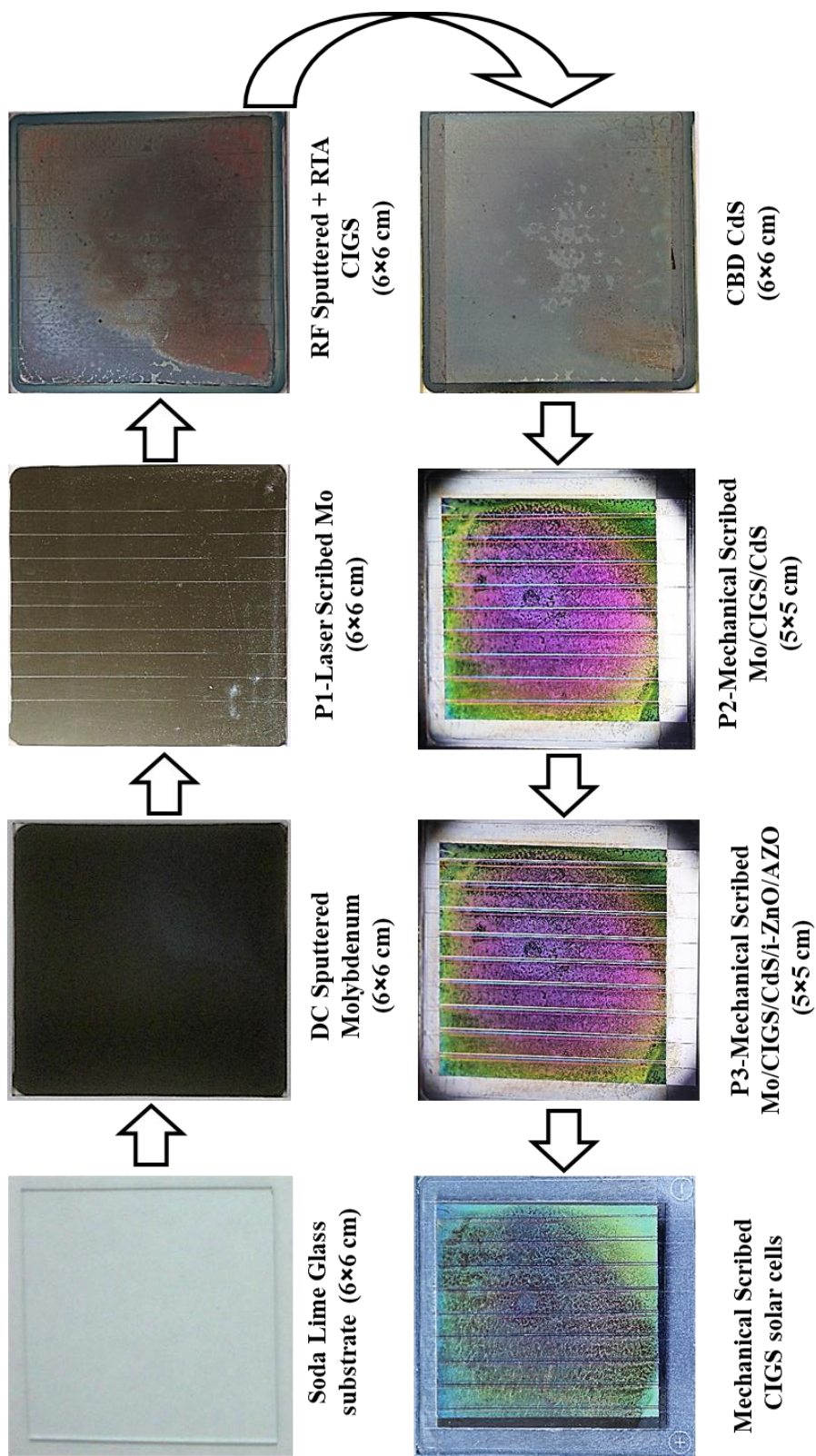


**Fig. 7.6: Fabrication steps of Monolithic integrated CIGS Solar Cell Module.**

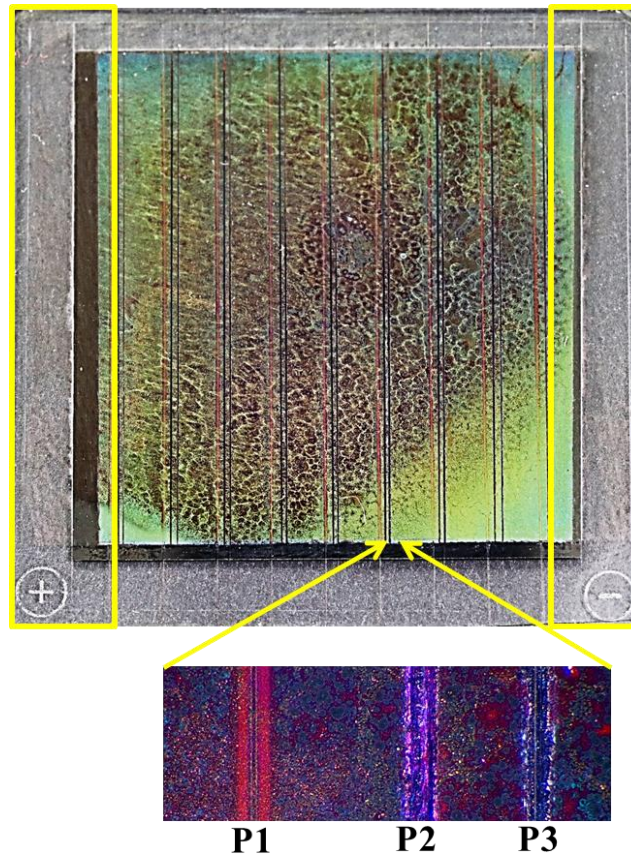


**Fig. 7.7: Close view of P1 laser patterned, P2 and P3 mechanical scribed multilayered CIGS solar cell module.**

## **7.2 Results and Discussion**

After the deposition of the thin-film CIGS solar cell module, analyzing its performance is a crucial task. Experimental set-up for performance analysis of cell and module is shown in Fig. 7.8. Keithley model 2420-C 3A and 2000 were used as source meter and multimeter. A Metal-halide lamp of 150 W AM 1.5 was used for an illuminating light source. The set-up was connected to a computer and data acquisition was carried out using LabView 2017 via GPIB. The performance of the CIGS thin-film solar cell was optimized with different buffer CdS layer deposition techniques, CdS layer deposited by CBD technique with different deposition duration, and an i-ZnO layer of different thickness. and CdS layer.

For good electrical transport losses in the photovoltaic device should be identified and rectified. There are three types of losses, one is optical which limits the generation of charge carriers which in turn reduces the overall device

current. The second is recombination losses which is limit the voltage and the third is parasitic losses which include the series and shunt resistance and voltage-dependent current collection. Parasitic losses have not only affects the fill factor but may be responsible for Voc and Isc reduction [3].

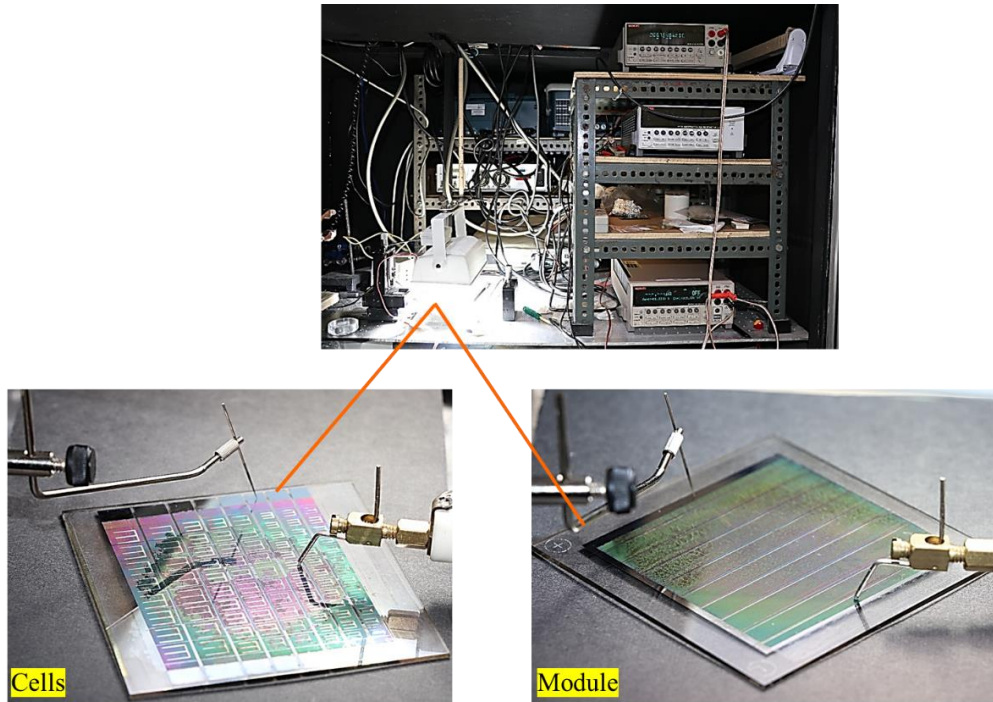
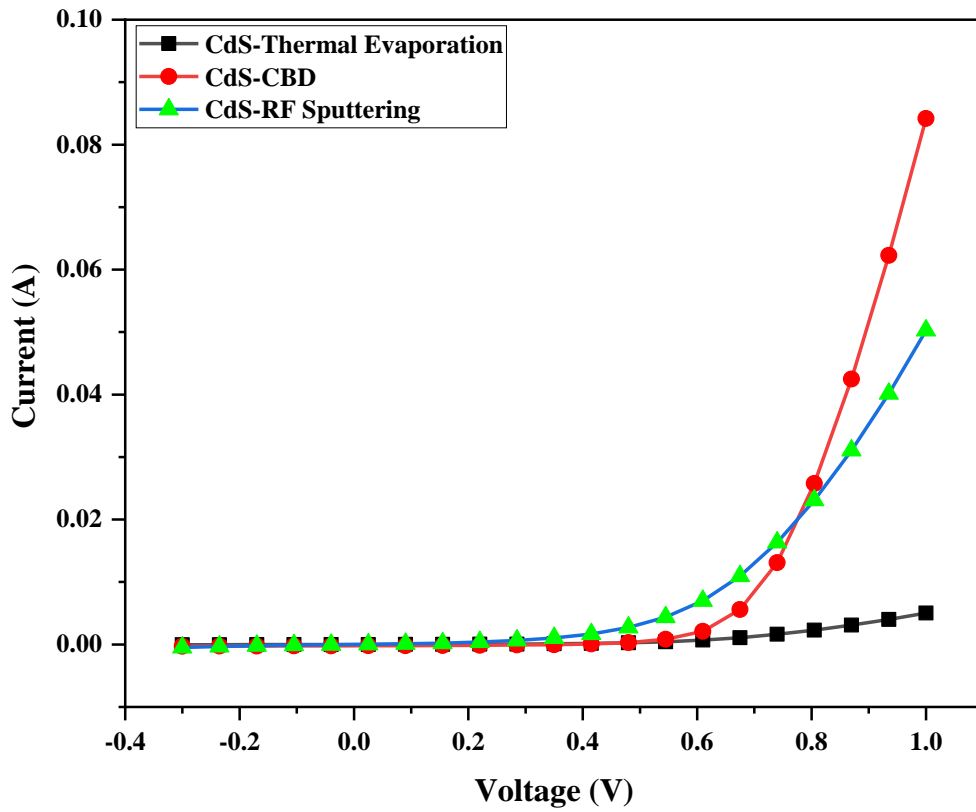
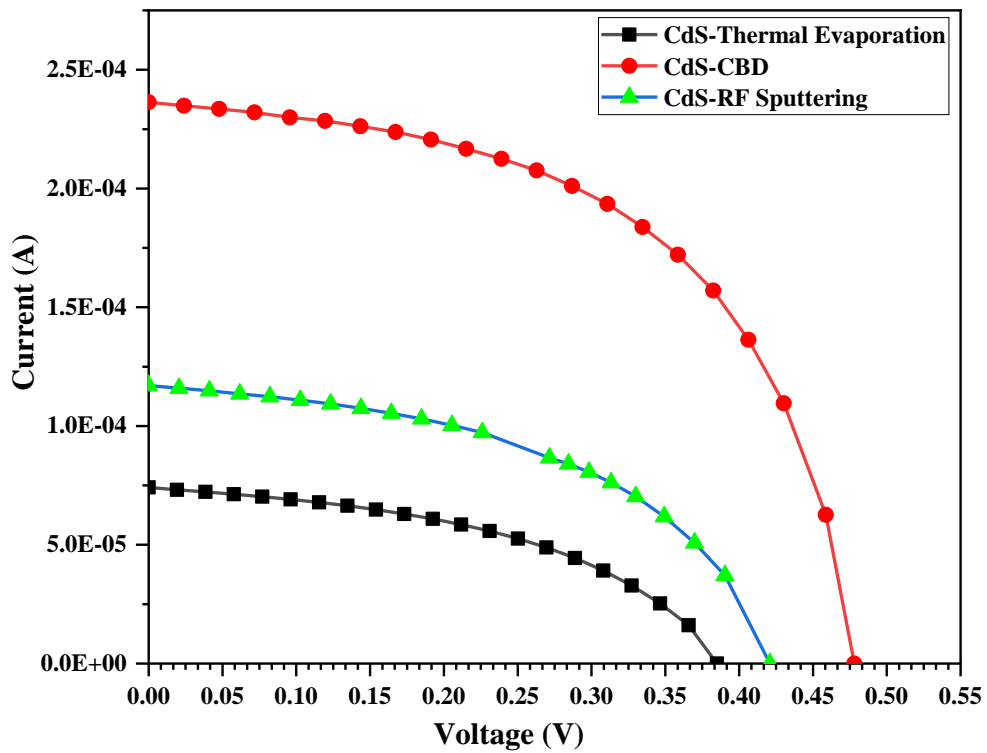


**Fig. 7.8: Experimental Set-up for performance analysis of multilayered CIGS solar cell module.**

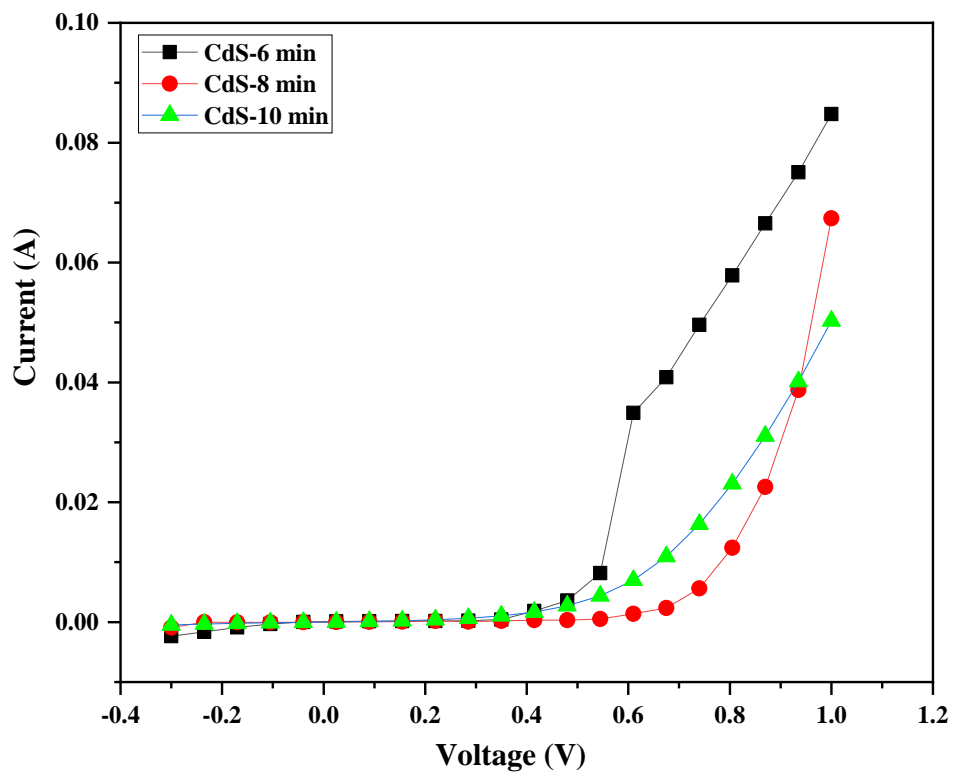
The electrical transport properties are governed by barrier height between conduction and valence band at the interface of two layers. To reduce the recombination cliff in the conduction band should be avoided as well as spike of more than 400 meV will reduce the device's performance. Hence, interface recombination will take place.



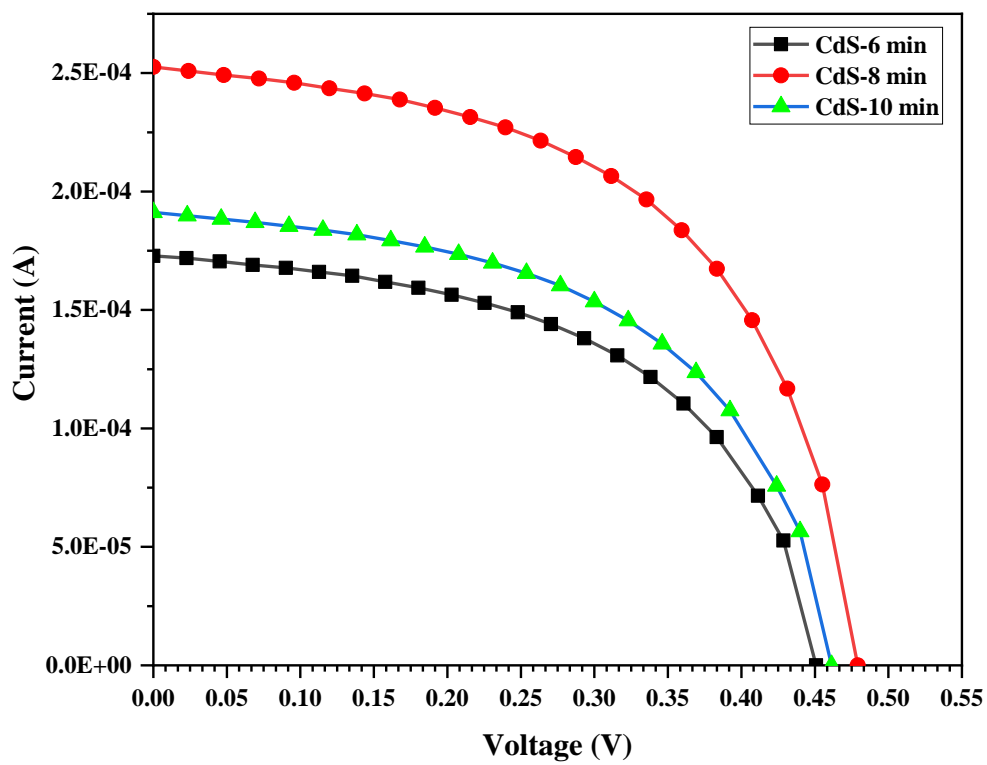
(a)



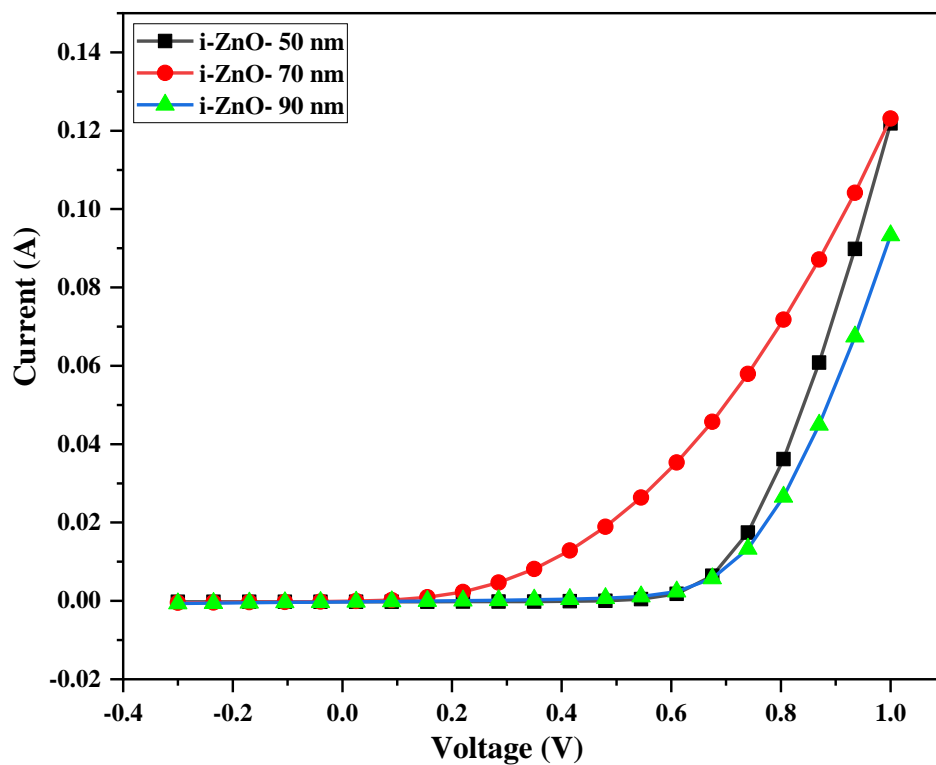
(b)



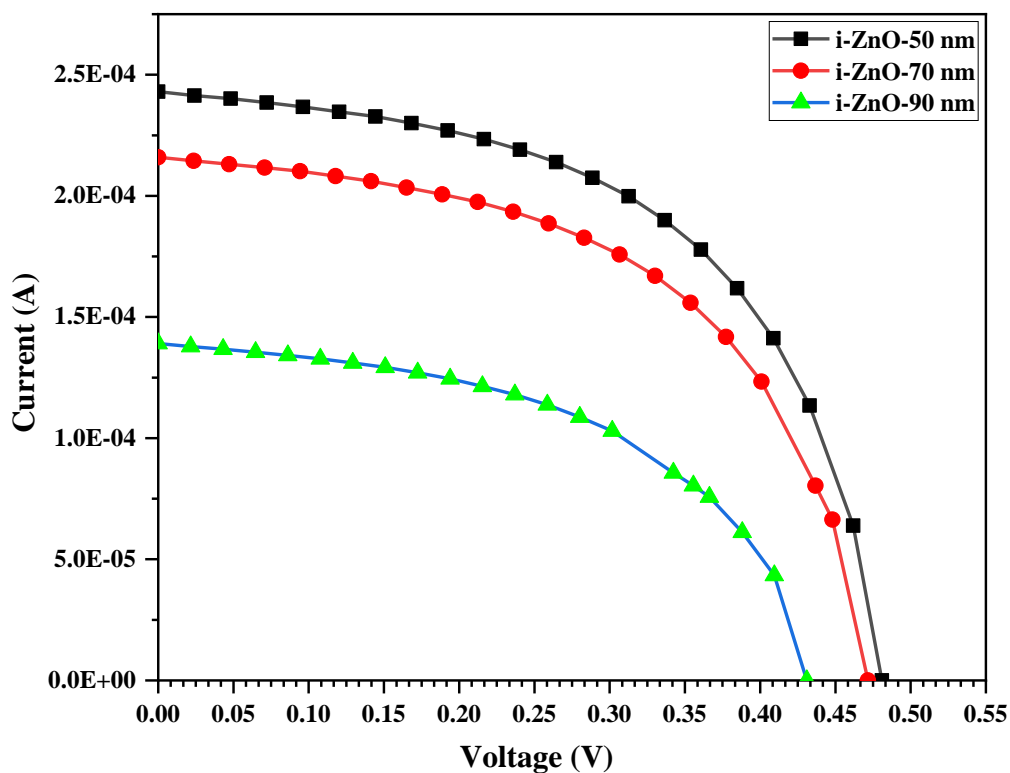
(c)



(d)



(e)



(f)

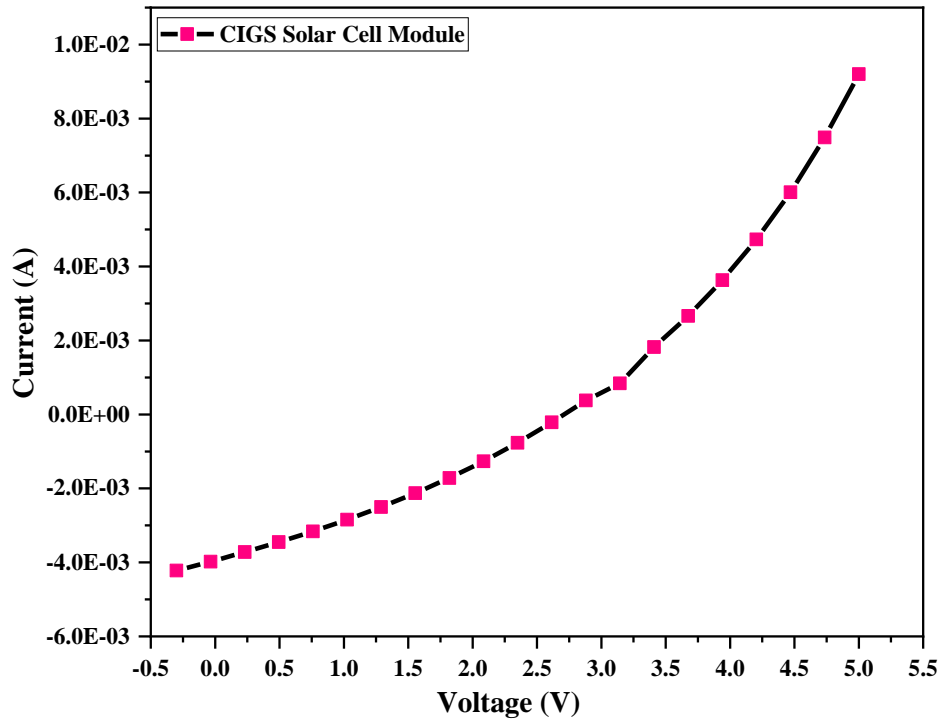
**Fig. 7.9: Dark and under-illumination I-V curve of (a, b)-CdS by a different deposition technique, (c, d)-CdS-CBD for different duration of deposition, and (e, f)-i-ZnO layer with different thickness.**

Fig. 7.9 (a) and (b) represent dark and under-illumination (light) I-V curves of CIGS solar cells with CdS deposited with different techniques. The slope of the dark I-V curve is large for CdS-thermal evaporation and CdS-RF sputtering, while the slope is reduced in CdS-CBD. Thermal evaporation and RF sputtering technique induce the intermixing of Cu and Cd at the CIGS/CdS junction [4, 5]. Thus, the barrier height increases which leads to band discontinuities. There is a rise in the positive conduction band (spike) which limits the charge carrier transport. In the case of CdS-CBD, negligible band bending has occurred due to which no distortion in the dark I-V curve was observed [6]. The growth of CIGS has a non-uniformity growth with indium rich surface which may contribute to the distortion. CdS-CBD technique etches the CIGS surface and removes the native oxide which enhances the epitaxial growth. Under illumination, CdS-CBD draws  $I_{sc} = 0.2$  mA and  $V_{oc} = 480$  mV. Fig 7.9 (c) and (d) represent the dark and light I-V curves of CIGS solar cells with different CdS layers deposited for a different duration. From Fig. 7.9 (c), the CdS layer deposited for 6 min possesses a mixed response of the I-V curve. A threshold was observed around 510 mV, but the response of the I-V curve gets distorted showing a resistive nature. Such response may be due to non-uniform grain growth distribution. Increasing the duration of deposition to 8 min, the non-distorted I-V curve was observed. Whereas a further increase in the duration of CdS deposition to 10 min, the slope of the I-V curve increases, and slight distortion were observed. 10 min deposition duration may have reached saturation of lateral grain growth due to which band-bending occurs at the interface [7, 8]. Under illumination, CdS-CBD deposited for 8 mins performs well compared to the other two. Fig. 7.9 (e) and (f) represent the dark and I-V curves of i-ZnO of thickness 50 nm, 70 nm, and 90 nm. The role of i-ZnO in device performance is still a debate. According to research findings, the i-ZnO layer protects the absorber and buffer layer by the impact of high energetic sputter AZO atoms and another role is to reduce the bandgap discontinuity. Too low thickness will give rise to the bandgap discontinuity, whereas an increase in thickness will weaken the built-in field. Less distortion of the I-V curve was observed for i-ZnO 50 nm, whereas an increase in thickness leads to the distortion [9]. Compare to i-ZnO 90 nm band-bending was more than i-ZnO 70

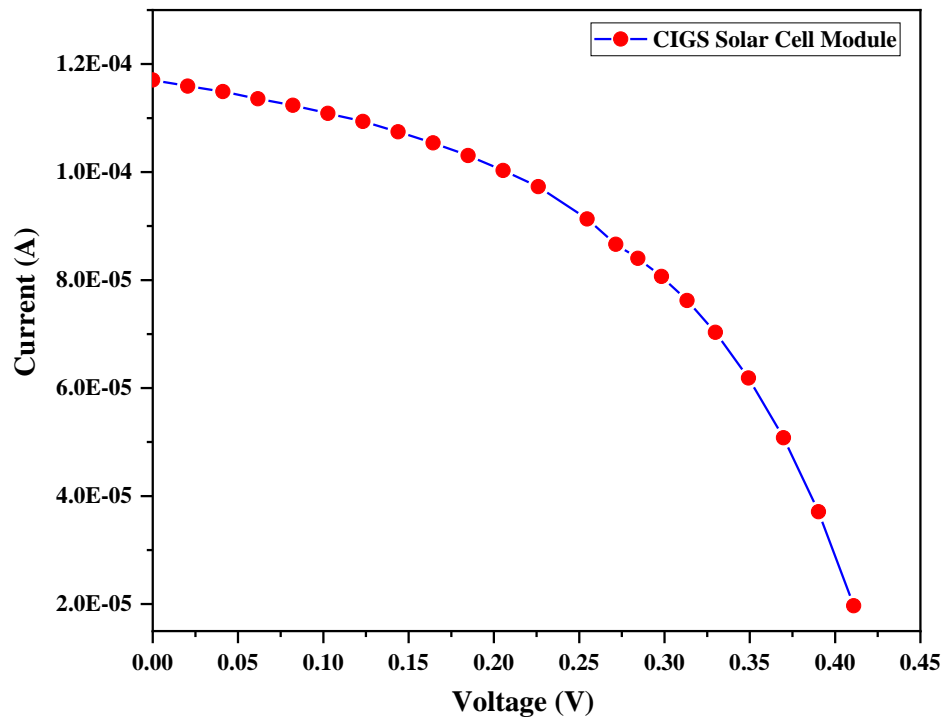
nm. This reflects the inadequate amount of majority carrier concentration within i-ZnO 70 nm. One can conclude that the effect of the i-ZnO layer on the performance of the CIGS solar cell is not thickness-dependent but rather it is carrier concentration-dependent. The performance parameters have been extracted from the above I-V curves and mentioned in Table 7.2.

**Table 7.2: The performance parameters have been extracted from the above I-V curves**

<b>Sample</b>	<b>V<sub>oc</sub> (mV)</b>	<b>I<sub>sc</sub> x 10<sup>-4</sup> (A)</b>	<b>Efficiency (η %)</b>	<b>Fill Factor</b>	<b>Rs (Ω-cm<sup>2</sup>)</b>	<b>Rsh (Ω-cm<sup>2</sup>)</b>
<b>CdS- Thermal</b>	385	0.74	0.14	46	2655	12197
<b>CdS-CBD</b>	478	2.36	0.68	54	796	6992
<b>CdS-RF sputtering</b>	415	1.16	0.27	51	1913	10056
<b>i-ZnO-50 nm</b>	481	2.43	0.71	54	773	6985
<b>i-ZnO-70 nm</b>	471	2.16	0.61	54	994	8208
<b>i-ZnO-90 nm</b>	430	1.39	0.34	51	1581	9868
<b>CdS-6 min</b>	450	1.73	0.45	52	1257	8969
<b>CdS-8 min</b>	479	2.53	0.73	54	747	6557
<b>CdS-10 min</b>	461	1.91	0.52	53	1135	8585



(a)



(b)

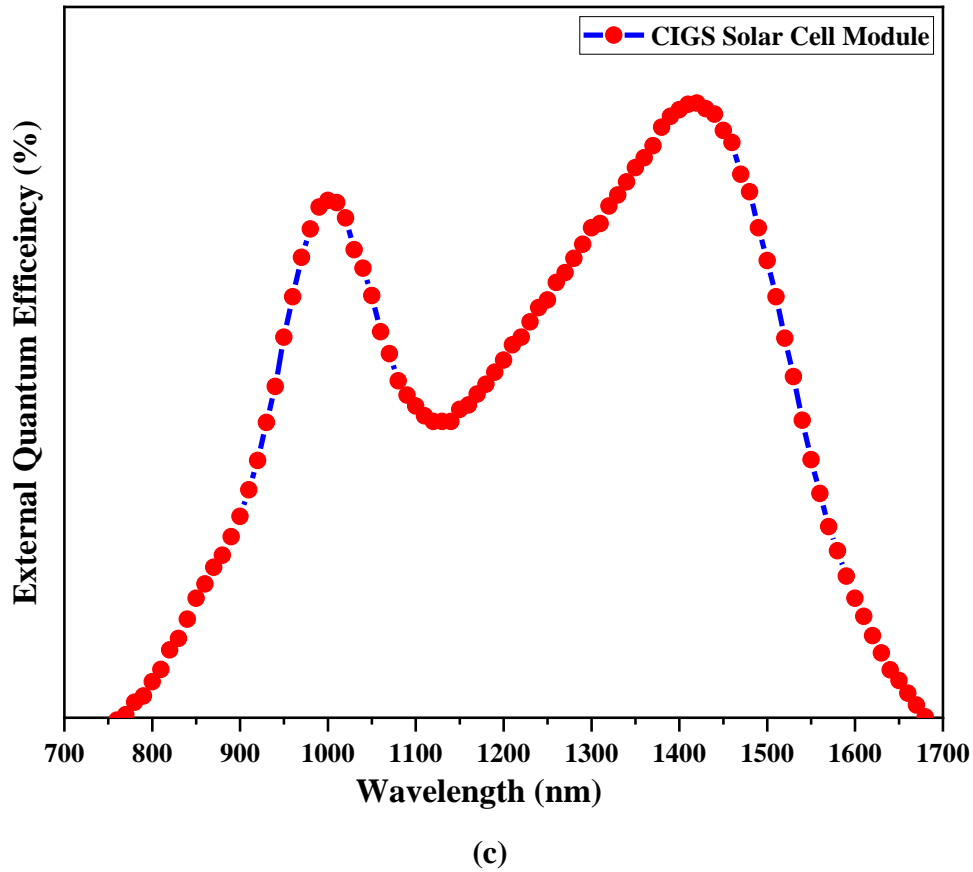


**Fig. 7.10: (a) Dark, (b) Under-illumination I-V curve, and (c) Quantum Efficiency of CIGS Solar Cell module.**

Fig. 7.10 (a), (b), and (c) represent dark, under-illumination I-V curve and quantum efficiency of 50 x 50 mm CIGS solar cell module. The Dark I-V curve shows the leakage current, and the nature of the curve represents the resistive loss, inhomogeneities in layers, recombination in bulk, space charge region, and at the interface. Also, monolithic integration contributes to the reduction of device performance. Under illumination, the I-V curve draws attention to the presences of the shunt losses, series losses, lattice-mismatch, and shading losses. The device draws  $I_{sc} = 0.11 \text{ mA}$ ,  $V_{oc} = 410 \text{ mV}$ , efficiency ( $\eta \%$ ) = 0.26,  $FF = 50$ ,  $R_s = 1879 \text{ } \Omega\text{-cm}^2$  and  $R_{sh} = 9062 \text{ } \Omega\text{-cm}^2$ . Fig. 7.10 (c) shows the quantum efficiency of 50 x 50 mm of CIGS solar cell module. The overall reduction in quantum efficiency is due to reflection and the low diffusion length of the charge carrier. The blue response is reduced to top window layer recombination. At higher wavelength there is insufficient absorption may be due to low thickness or inhomogeneities of absorber CIGS layer. Incomplete

generation and collection of charge carriers also leads to a decrease in the quantum efficiency. Modules have larger area compared to laboratory cells, thus longer electrical path over the module area may results into reduction of electrical resistance. Therefore, monolithic integration of module at three levels P1, P2, and P3 have crucial importance for high power conversion efficiency [13].

## Conclusions

This chapter concludes the fabrication process step for developing CIGS solar cells. CIGS solar cell with different Al-Finger grids size was fabricated. The cell to module fabrication process was optimized using PVD and the Chemical Bath deposition technique. Monolithic integration at three levels (P1) with Nd:YAG 1064 nm and (P2, P3) with mechanical scribing was carried out. The performance of CIGS solar cells with different deposition conditions was optimized. CdS-buffer layer deposited by CBD technique for 8 min has more charge extraction. Optimizing the i-ZnO layer of different thicknesses, the results state the performance of the cell is not dependent on thickness but rather on the charge density of the i-ZnO layer. CIGS solar cell module of 50 x 50 mm was fabricated, and its performance was analyzed. Loss in quantum efficiency was observed to be due to incomplete absorption at a longer wavelength and recombination at the front end of the device.

## References

- [1] Michael Powalla, Stefan Paetel, Dimitrios Hariskos, Roland Wuerz, Friedrich Kessler, Peter Lechner, Wiltraud Wischmann, and Theresa Magorian Friedlmeier, *Engineering*, **3 (4)** (2017) 445-451.
- [2] Aiko Narazaki, Tadatake Sato, Hiroyuki Niino, Hideyuki Takada, Kenji Torizuka, Jiro Nishinaga, Yukiko Kamikawa-Shimizu, Shogo Ishizuka, Hajime Shibata, and Shigeru Niki, *Laser Applications in Microelectronic and Optoelectronic Manufacturing (LAMOM) XXII*, **10091** (2017) 100911E-1- 00911E-9.
- [3] William N. Shafarman and Lars Stolt, *Handbook of Photovoltaic Science and Engineering*, John Wiley & Sons (2003).

- [4] Xiaoqing He, Peter Ercius, Joel Varley, Jeff Bailey, Geordie Zapalac, Tim Nagle, Dmitry Poplavskyy, Neil Mackie, Atiye Bayman, Vincenzo Lordi, and Angus Rockett, *Prog Photovolt Res Appl.*, (2018) 1-9.
- [5] Sławomir Gułkowski, and Ewelina Krawczak, *E3S Web of Conferences*, **19** (2017) 03006 (1-6).
- [6] Soon Mi Park, Tae Gun Kim, Yong Duck Chung, Dae-Hyung Cho, Jeha Kim, Kyung Joong Kim, Yeonjin Yi and Jeong Won Kim, *J. Phys. D: Appl. Phys.*, **47** (2014) 345302 (1-8).
- [7] L. Weinhardt, O. Fuchs, D. Groß, G. Storch, E. Umbach, N. G. Dhere, A. A. Kadam, S. S. Kulkarni, and C. Heske, *Appl. Phys. Lett.*, **86** (2005) 062109-1-062109-3.
- [8] Dieter Schmid, Martin Ruckh, and Hans Werner Schock, *Solar Energy Materials and Solar Cells*, **41/42** (1996) 281-294.
- [9] Salh Alhammadi, Hyeonwook Park and Woo Kyoung Kim, *Materials*, **12** (2019) 1365 (1-16)
- [10] Anant H. Jahagirdar, Ankur A. Kadam and Neelkanth G. Dhere, *IEEE 4th World Conference on Photovoltaic Energy Conference, Waikoloa, HI*, (2006) 557-559.
- [11] Fredrik Larsson, Jan Keller, Marika Edoff, and Tobias Törndahl, *Thin Solid Films*, **633** (2017) 235-238.
- [12] S. Dongaonkar, J. D. Servaites, G. M. Ford, S. Loser, J. Moore, R. M. Gelfand, H. Mohseni, H. W. Hillhouse, R. Agrawal, M. A. Ratner, T. J. Marks, M. S. Lundstrom, and M. A. Alam, *Journal of Applied Physics*, **108** (2010) 124509-1- 124509-10.
- [13] Ju-Heon Yoon, Jong-Keuk Park, Won Mok Kim, JinWoo Lee, Hisun Pak & Jeung-hyun Jeong, *Sci Rep* **5** (2015) 7690 (1-9).